Chemical Science

ROYAL SOCIETY OF CHEMISTRY

EDGE ARTICLE

View Article Online
View Journal | View Issue

Cite this: *Chem. Sci.*, 2024, **15**, 5973

All publication charges for this article have been paid for by the Royal Society of Chemistry

Rational design of CT-coupled J-aggregation platform based on Aza-BODIPY for highly efficient phototherapy†

Shengmei Wu,‡[a] Wenze Zhang,‡[b] Chaoran Li,[b] Zhigang Ni,[a] Weifeng Chen,[a] Lizhi Gai,*[a] Jiangwei Tian,*[b] Zijian Guo[c] and Hua Lu*[a]

Supramolecular engineering is exceptionally appealing in the design of functional materials, and J-aggregates resulting from noncovalent interactions offer intriguing features. However, building J-aggregation platforms remains a significant challenge. Herein, we report 3,5-dithienyl Aza-BODIPYs with a donor–acceptor–donor (D–A–D) architecture as the first charge transfer (CT)-coupled J-aggregation BODIPY-type platform. The core acceptor moieties in one molecule interact with donor units in neighboring molecules to generate slip-stacked packing motifs, resulting in CT-coupled J-aggregation with a redshifted wavelength up to 886 nm and an absorption tail over 1100 nm. The J-aggregates show significant photoacoustic signals and high photothermal conversion efficiency of 66%. The results obtained *in vivo* show that the J-aggregates have the potential to be used for tumor photothermal ablation and photoacoustic imaging. This study not only demonstrates Aza-BODIPY with D–A–D as a novel CT-coupled J-aggregation platform for NIR phototherapy materials but also motivates further study on the design of J-aggregation.

Received 28th December 2023
Accepted 26th February 2024

DOI: 10.1039/d3sc06976a

rsc.li/chemical-science

Introduction

With the advancement of optical diagnosis and nanomedicine, near-infrared organic dyes have demonstrated tremendous promise in the fields of disease diagnosis and phototherapy.[1] Molecular engineering has been a widely used strategy to develop NIR dyes with desired properties.[2] In addition to the molecular engineering strategy, supramolecular engineering offers an alternative approach for the design of NIR dyes by forming J-type aggregates.[3] This strategy takes advantage of the exchange narrowing effect between chromophores, which can lead to a significant redshift in the absorption wavelength.[4] J-aggregation has emerged as a convenient method to achieve NIR absorbance.[4c] However, the construction of J-aggregates is usually developed by serendipitous discovery, and the rational design of molecular structures to induce J-aggregation of organic dyes remains a challenge. Although there have been successful examples of J-aggregate formation, developing a systematic and predictable approach for designing J-aggregates is still an ongoing area of research.[4b,d,5]

Classical J-aggregation refers to the accumulation of dye molecules in a slip-stacked manner along the direction of the dipole moment, with the slip angle of $\theta < 54.7°$. This phenomenon leads to a narrow absorption peak in J-aggregation under the influence of the long-range Coulomb coupling. Typically, there is a wavelength shift of around 30 nm,[6,7] which is limited to controlling the wavelength red shift. In addition, the narrow absorption peak (usually FWHM <40 nm) causes an unsatisfactory matching between the laser wavelength and absorption peak, making the selection of appropriate lasers for phototherapy difficult. Therefore, the development of J-aggregates with superior spectral characteristics has become an urgent matter. In D–A–D architectures, slip-stacked packing motifs are favored, where the central acceptor moiety in one molecule interacts with donor moieties in neighboring molecules (Fig. 1).[4c,8] The particular arrangement of these interactions can result in different types of spectra with J-Coulomb dominance (conventional J-aggregation) or CT-coupled J-aggregation, the latter of which might even have an H-type J-Coulomb component.[8,9] The mixing of multiple couplings results in band widening, which helps match lasers and is required for panchromatic light absorption. Currently, several CT-coupled J-aggregates based on the D–A–D

[a]*College of Material, Chemistry and Chemical Engineering, Key Laboratory of Organosilicon Chemistry and Material Technology, Ministry of Education, Hangzhou Normal University, No. 2318, Yuhangtang Road, Hangzhou, 311121, P. R. China. E-mail: lizhigai@hznu.edu.cn; hualu@hznu.edu.cn*

[b]*State Key Laboratory of Natural Medicines, Jiangsu Key Laboratory of TCM Evaluation and Translational Research, School of Traditional Chinese Pharmacy, China Pharmaceutical University, Nanjing 211198, P. R. China. E-mail: jwtian@cpu.edu.cn*

[c]*State Key Laboratory of Coordination Chemistry, Coordination Chemistry Institute, School of Chemistry and Chemical Engineering, Nanjing University, Nanjing 210023, P. R. China*

† Electronic supplementary information (ESI) available. See DOI: https://doi.org/10.1039/d3sc06976a

‡ These authors contributed equally to this work.

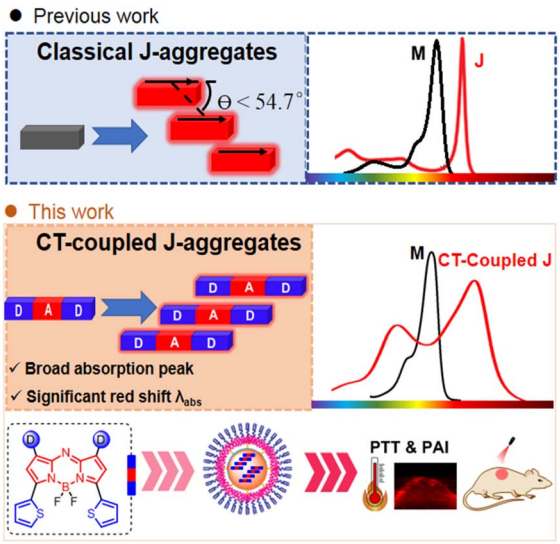

Fig. 1 Creation of CT-coupled J-aggregates. Schematic illustration of classical J-aggregates and strategic design of CT-coupled J-aggregates in this study.

architecture are limited to the squaraine system.[10] The electron-deficient aza-BODIPY core is an ideal model to construct a D–A–D structure to form a slip-stacked packing motif.[11] Recent studies have reported several aza-BODIPY dyes with conventional J-aggregation,[12] in which main driving forces for aggregation are diverse, such as hydrogen bond,[13] solvophobic interactions[14] and π–π stacking interactions.[15] Despite these advancements, there is still much to explore in the rational design and stabilization of J-aggregates. Herein, we present a general D–A–D scaffold incorporating thiophene units as donors[16] into the 3,5-position of aza-BODIPY to construct CT-coupled J-aggregates. The resulting thiophene(D)–aza-BODIPY(A)–D scaffold exhibits hypsochromic and bathochromic absorption bands, corresponding to the mixing between intermolecular CT and Frenkel states due to pronounced D–A interaction. Moreover, the CT-coupled J-aggregates were demonstrated to be applicable to photoacoustic (PA) imaging-guided photothermal therapy (PTT).

Results and discussion

Molecular design

Slip-stacked packing motifs are highly favored in the D–A–D architecture. The aza-BODIPY core is an ideal acceptor due to its planar electron-deficient properties. The donor moiety at the 3,5-position plays a crucial role in forming the CT-coupled J-aggregates because the electronic effect at the 3,5-position contributes to HOMO and LUMO orbitals (Fig. S1 and Table S1†).[17] The five-ring thiophene unit is a wonderful candidate with electron-rich nature. In addition, the angle between the five-ring thiophene (D) and aza-BODIPY core is smaller than that of the six-ring donor. This smaller angle facilitates increased conjugation and interaction between the donor and acceptor moieties, which is beneficial for the formation of the CT-coupled J-aggregates. Taking advantage of the unique properties of thiophenes, we developed a series of 3,5-dithienyl (D1)–aza-BODIPY(A)–D2 structures (Fig. 2A). These compounds are loaded with different electron-donor groups at the 1,7-position to achieve general CT-coupled J-aggregation. Additionally, D–A–A structures were designed to gain a deeper understanding of the aggregate characteristics.[18] The synthesis of **BDP1–5** adopts the classic Aza-BODIPY synthesis method.[18a,19] The detailed synthesis process and characterization information are in the ESI.†

Spectroscopic properties

We first investigated the spectroscopic properties of dichloromethane (Fig. 2B and Table S2†). **BDP1–5** exhibited strong absorption spectra with a large molar extinction coefficient (3–7.5 × 10^4 M^{-1} cm^{-1}) and maximum wavelength covering the 717–786 nm region through the modification of the substituent at the 1,7-position. The strong electron-donating *N*,*N*-dialkyl groups resulted in the splitting of the maximum absorption into two parallel peaks. This split can be attributed to the presence of local excitation (LE) and charge transfer (CT) transition states. Photobleaching resistance is a crucial property. The maximum absorption of **BDP1–5** exhibits minor change within 2%, whereas control indocyanine green (ICG) was significantly reduced after 30 min of irradiation (Fig. S2†), indicating their promising photobleaching resistance.

We then investigated the aggregation behavior. The dyes were first dissolved in THF and later quickly injected into water containing DSPE-PEG2000 under stirring, leading to the formation of micellar nanoparticles (Fig. S3†). The UV/Vis spectra showed significant changes upon aggregation. D–A–D scaffolds **BDP2–4** display broad absorption spectra (FWHM = 205 nm for **BDP2**, 209 nm for **BDP3**, and 298 nm for **BDP4**) with two distinguishable maxima with H-type $J_{Coulomb}$ and pronounced donor–acceptor interaction between monomers due to a significant HOMO–LUMO overlap (Fig. S1†). The energetically low-lying charge transfer (CT) states interact with Frenkel states, resulting in a mixing of electronic states. This mixing leads to the formation of optically allowed states at higher and lower energy compared to the monomer. In contrast, **BDP1** with a weak donor at the 1,7-position exhibited a weak H-type $J_{Coulomb}$ and strong short-range coupling owing to wavefunction overlap. The substituent group greatly disturbed the type of aggregation. The 3,5-position phenyl aza-BODIPY displayed a minor absorptive change before and after aggregation, indicating that substituents at the 3,5-position have a significant effect on the formation of J-aggregation (Fig. S4†). In the case of the D–A–A structure, a blue-shifted and broad absorption band was observed, since it is prone to self-assembly into an extended 1d card-stack arrangement with pronounced Coulomb H-coupling (Fig. 2B).

Crystal packing can provide valuable insights into the aggregation behavior of molecules (Fig. 2C). According to the analysis of the X-ray structures of **BDP1–2**,[18a] they possess a rigid π system from B–F···H–C (thiophene) hydrogen interaction by inhibiting the rotation of thiophene. In the context of **BDP1**, it can be observed that the overlap between two parallel molecules

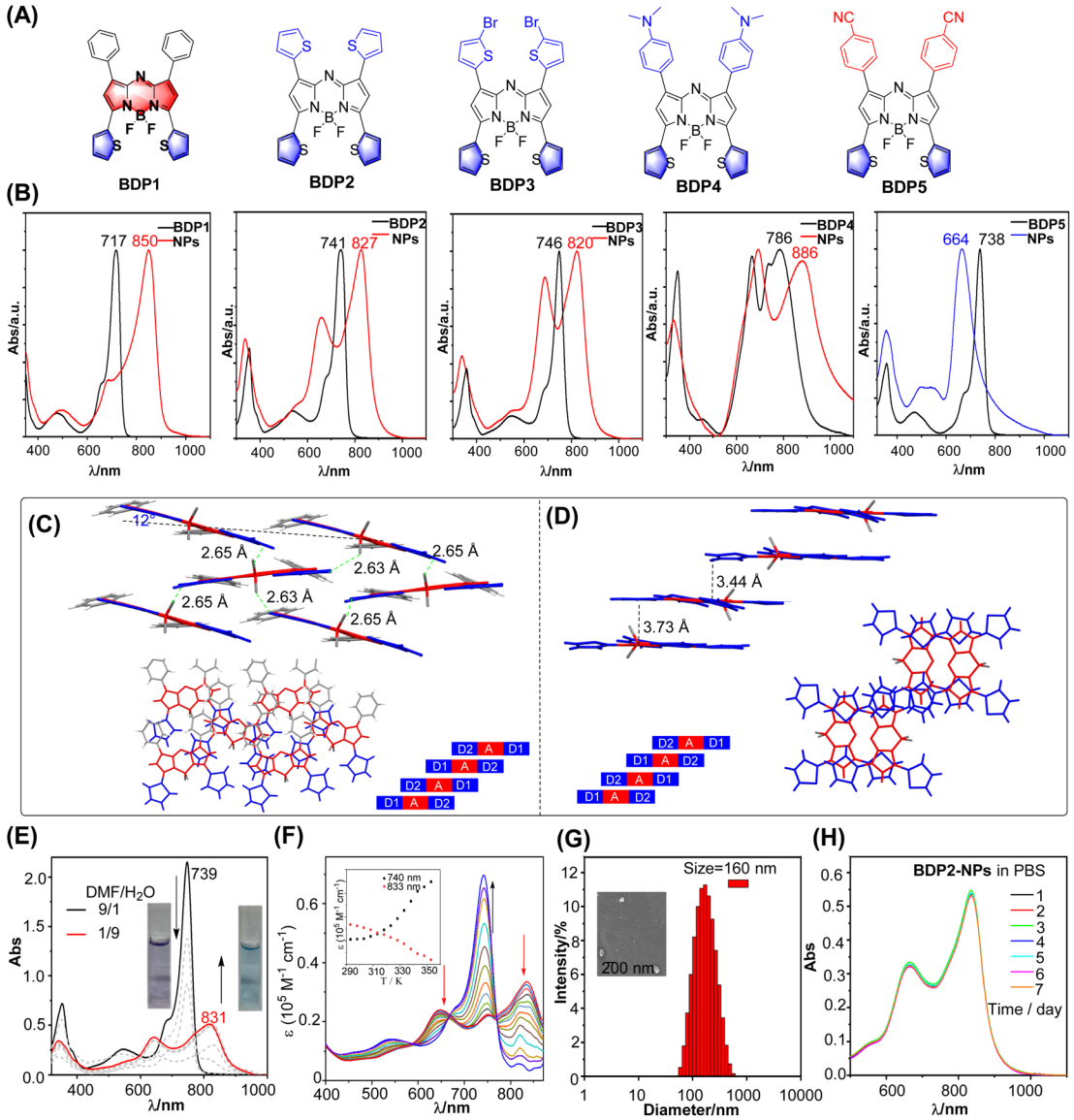

Fig. 2 (A) Structure of **BDP1–5**. (B) Comparison of the absorption of **BDP1–5** in THF and **BDP1–5 NPs** in water. (C and D) Molecular structure of **BDP1** (left) and **BDP2** (right) in the single crystal state with the F···H (thiophene) bond, packing motif in the single-crystal structure, and a schematic depiction of extended, antiparallelly aligned π-stacks, respectively. CCDC no. 877767 and 877768. Reproduced from ref. 18a with permission. (E) Absorption spectra of **BDP2** in a DMF/water mixture with different water fractions. Inset: natural light image of **BDP2** in DMF/water (1/9 and 9/1). (F) Temperature-dependent absorption spectra of **BDP2** in a DMF/water (3/2) mixture from 293 to 353 K at a total concentration of 10 μM. (G) The size distribution of **BDP2-NPs** using DLS at 298 K. (H) Absorption spectra of **BDP2-NPs** in PBS for different days.

is less pronounced, while there is a relatively higher degree of overlap with the neighboring molecules. This increase in overlap is primarily attributable to intermolecular interactions that arise between the electron-donating thiophene unit and non-parallel parent nucleus of the adjacent molecule, as well as between the thiophene unit and parent nucleus of a distinct molecule. Such intermolecular forces in turn facilitate the effective aggregation of the molecules. In the case of **BDP2**, it can be observed that the intermolecular spacing between parallel molecules is restricted to 3.73 and 3.44 Å, leading to an evident intermolecular π–π interaction.[19] When examining the crystal packing from a top-down perspective, the presence of an electron-donating thiophene unit and another parallel electron-deficient core of the molecule is observed to play a significant role in this process. Overall, the crystal packing structure confirms the plausibility of utilizing a D–A–D strategy to facilitate the aggregation of molecules and intermolecular interactions.

To gain insight into the detailed aggregation state-related physiochemical properties, the absorption spectra of **BDP2** under different DMF/water ratios were investigated, with the addition of water leading to a gradual decrease in the main absorption peak and appearance of a new absorption peak at 831 nm for **BDP2** (Fig. 2E). Subsequently, the absorption peak of the monomer with maximum absorption of 739 nm increased on increasing the temperature from 293 K to 353 K, and this result

verified that the self-assembly was reversible (Fig. 2F). We conducted an investigation into the aggregation mechanism of **BDP2** employing a nucleation–elongation model.[20] By analyzing the Vis-NIR spectral data and fitting resulting curves, we determined the fraction of aggregated molecules (α_{Agg}), temperature (T), molar enthalpy (ΔH_e), and elongation temperature (T_e) (Fig. S5†). Our analysis revealed a molar enthalpy change of −18.2 kJ mol^{-1} and an elongation temperature of 360 K. Notably, the lower molar enthalpy indicates that **BDP2** exhibits a higher aggregation propensity, suggesting its ease of aggregation. SEM was used to test its aggregates and confirmed that it formed a large number of the nanoparticles (Fig. S6a†).

Photothermal properties of BDP2-NPs

To ensure that **BDP2** has good water solubility and stability, we performed a comparative characterization of the structure of the encapsulated nanoparticles. The hydrodynamic size of the **BDP2-NPs** measured by dynamic light scattering (DLS) was around 160 nm (Fig. 2G), which contributed to their accumulation at tumor sites through the enhanced permeability and retention effect,[21] and their hydrodynamic diameters hardly changed after storage in a refrigerator at 4 °C for one week under normal physiological conditions (Fig. 2H, S6b and c†). While **BDP2-NPs** do not exhibit fluorescence emission due to the aggregation of free molecules in the nanoparticles, this property helps to improve their photothermal conversion ability, making them promising in photoacoustic/photothermal imaging and photothermal therapy.

Based on the fact that **BDP2-NPs** exhibit negligible fluorescence emission in water, it is inferred that the excitation energy can be released through a non-radiative decay process.[19a] Therefore, we investigated whether the **BDP2-NPs** are an effective reagent in photothermal water media (Fig. 3). The temperature changes of the **BDP2-NPs** at different concentrations were monitored upon laser irradiation. Following 600 s of 808 nm laser irradiation at 0.96 W cm^{-2}, the temperature difference increased by more than 25 °C for 30 μM **BDP2-NPs**. Positive correlations between the photothermal conversion efficiency of the **BDP2-NPs** and their concentration and laser power were found, indicating the controllable photothermal conversion behavior (Fig. 3a and b). Based on the photothermal effect and time constant,[22] the photothermal conversion efficiency of the **BDP2-NPs** was calculated to be 66% (Fig. 3c). After five cycles of laser irradiation, the heating temperature of the **BDP2-NPs** remained stable at around 63 °C, indicating that the **BDP2-NPs** possess excellent photothermal properties (Fig. 3d). Subsequently, the temperature of the **BDP2-NP** solution increased from 25 °C to 56 °C after 5 min of laser irradiation, while only a minor temperature change was observed in the PBS reference (Fig. 3e). As compared to **BDP2-NPs**, **BDP1-NPs** possess similar PTT properties with a PCE value of 53% (Fig. S7†). Moreover, the **BDP2-NPs** produced the highest photoacoustic signal at 820 nm under 808 nm laser irradiation, indicating that the strong near-infrared absorption of the J-aggregate controlled the photoacoustic response.

The photoacoustic signal intensity displayed a linear correlation with concentration along with a correlation coefficient of 0.9808 (Fig. 3f and g). In addition, neither the **BDP1-NPs** nor **BDP2-NPs** were able to generate singlet oxygen, suggesting that this type of dye aggregates to produce a specific photothermal

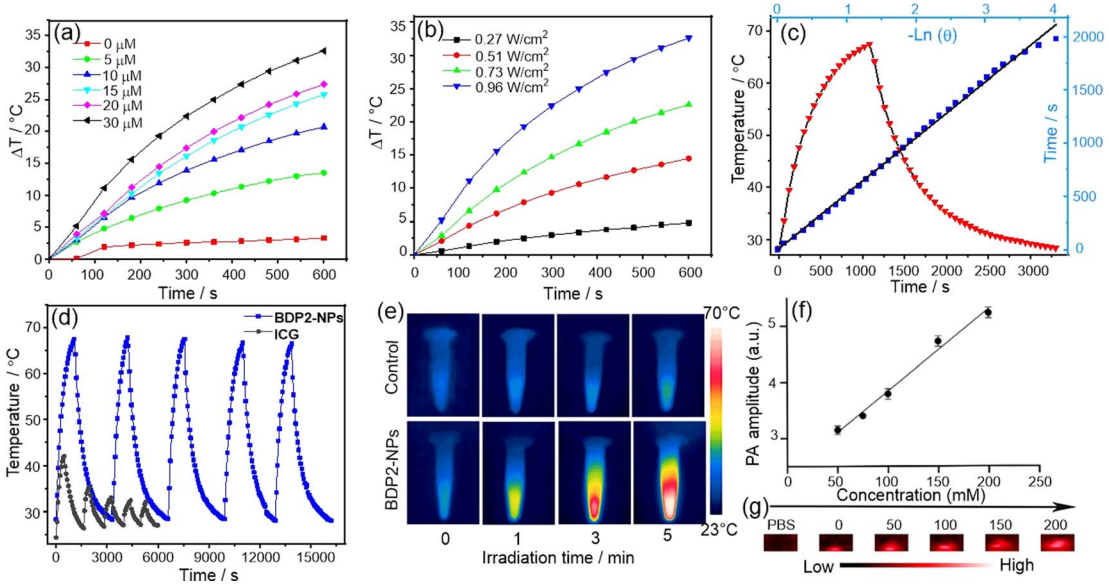

Fig. 3 (a) Heating curves of the **BDP2-NPs** at various concentrations upon laser irradiation (0.96 W cm^{-2}); (b) heating curves of the **BDP2-NPs** (30 μM) at increasing power density; (c) heating curves of the **BDP2-NPs** (30 μM) during a laser-on and off switching process, with the inset showing the related linear cooling time data *versus* −ln(θ). $\eta = 66\%$. (d) Heating and cooling curves of the **BDP2-NPs** (30 μM) upon five times laser irradiation (0.96 W cm^{-2}), with ICG (30 μM) as the control. (e) Photothermal imaging of the **BDP2-NPs** at different irradiation times. (f) Photoacoustic signals at 820 nm for different concentrations of the **BDP2-NPs**; data are presented as mean ± SD ($n = 3$). (g) Photoacoustic signals showing a proportional relationship with the **BDP2-NP** concentration.

reagent (Fig. S8†). Thus, the remarkable photoacoustic signal of the NPs meets the requirements of *in vivo* imaging and could be utilized in future *in vivo* PTT experiments.

Phototoxicity and biocompatibility

Afterward, we examined the photothermal therapy (PTT) efficacy of the **BDP2-NPs** in living cells. The classical MTT assay was utilized to study the biocompatibility and phototoxicity of the **BDP2-NPs** in Hepa 1-6 cells and HepG2 cells. The results (Fig. 4a) show that under normal conditions without a laser, the cell viability rate of the **BDP2-NPs** from 0 to 100 μM was almost always higher than 80%, suggesting their excellent biocompatibility. In contrast, under laser irradiation at lower power (0.1 W cm^{-2}), the rate of cell viability decreased significantly through the photothermal effect. In addition, fluorescence microscopy imaging was performed using Calcein AM/pyridine iodide (PI) dual staining to investigate the effect of the **BDP2-NPs** on cell survival (Fig. 4b). As the laser (0.2 W cm^{-2}) irradiation time increased, the red fluorescence (PI) gradually intensified, while the green fluorescence (Calcein AM) diminished, indicating the successful occurrence of excellent photothermal therapy (PTT). Flow cytometry analysis demonstrated that even at low laser power, after 8 min of laser (0.1 W cm^{-2}) irradiation, cell apoptosis could be induced by the photothermal effect effectively (Fig. S9†). These experiments certified that the **BDP2-NPs** possessed sufficient phototoxicity and biocompatibility for follow-up PTT.

BDP2-NP *in vivo* tumor PA imaging

The feasibility of the **BDP2-NPs** for *in vivo* PA imaging was then investigated. A weak PA signal was observed before **BDP2-NP** injection (0 h), attributed to the deoxygenated and oxyhemoglobin.[23] First, 100 μL of 100 μM the **BDP2-NPs** was injected into Hepa 1-6 tumor-bearing C57BL/6 mice through the tail vein, and PA images of tumors were recorded at different times (Fig. 4c and S10†). The photoacoustic signal of the **BDP2-NPs** in the tumors gradually increased after injection and reached a peak at 36 h, suggesting that the **BDP2-NPs** have good stability and significant tumor accumulation in blood circulation. These results indicated that **BDP2-NPs** can be used for photoacoustic imaging of in *vivo* tumors to precisely guide laser irradiation for photothermal therapy.

BDP2-NP *in vivo* tumor photothermal therapy

Encouraged by the great PA properties and outstanding tumor cell damage capability of the **BDP2-NPs** *in vitro* and *in vivo*, PA image-guided *in vivo* PTT was studied in Hepa 1-6 tumor-bearing C57BL/6 mice (Fig. 5). The tumor area of the mice was irradiated for 5 min using an 808 nm laser (0.2 W cm^{-2}) at 36 h after the tail vein injection of the **BDP2-NPs**. As shown in Fig. 5a, with the increase of the irradiation time, the

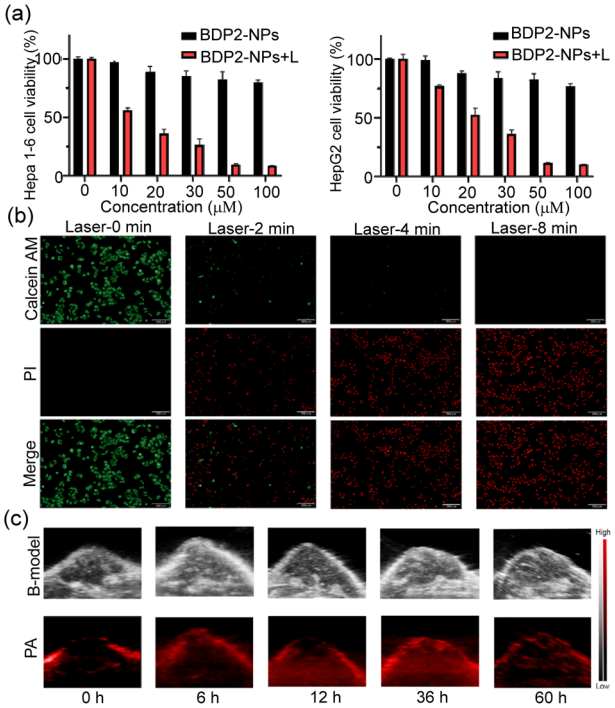

Fig. 4 (a) Cell viability of Hepa1-6 and HepG2 cells incubated with the **BDP2-NPs** at various concentrations in the dark and after laser irradiation (808 nm, 0.1 W cm^{-2}, 10 min); data are presented as mean ± SD (n = 5). (b) Photothermal induced apoptosis imaging by fluorescence microscopy. Scale bar: 200 μm. (c) Representative images of the ultrasound (US) and photoacoustic imaging of the **BDP2-NPs** in Hepa1-6 tumor-bearing mice.

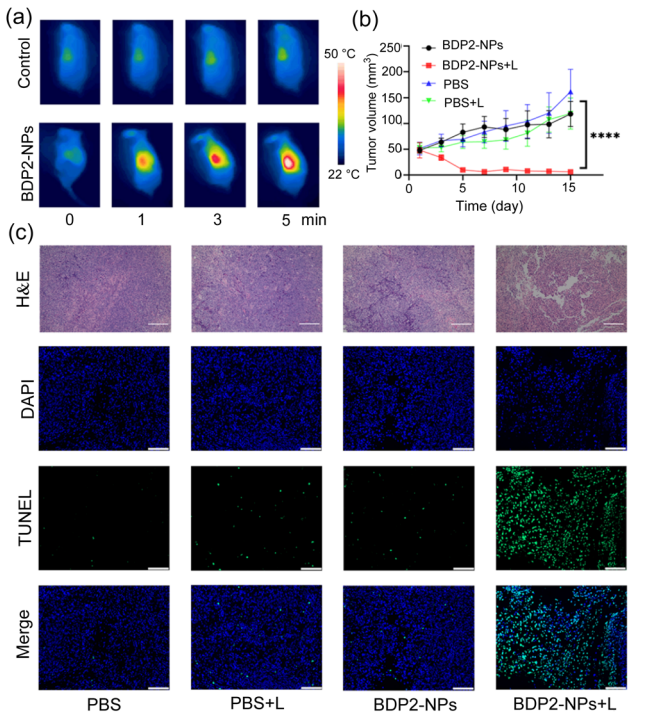

Fig. 5 (a) Representative thermographic images. (b) Tumor growth curves of various groups after different treatments; data are presented as mean ± SD (n = 4 mice). ****P < 0.0001. (c) H&E (scale bar: 200 μm) and TUNEL (scale bar: 20 μm) staining images in the tumor area of each group after various treatments.

temperature of the tumor area in the **BDP2-NP** group significantly increased to approximately 50 °C; however, the temperature in the control group which was injected with PBS did not change notably. To investigate the apoptosis of cancer cells induced by PTT *in vivo*, mouse tumor tissues were harvested for hematoxylin and eosin (H&E) staining and TUNEL (terminal deoxynucleotidyl transferase dUTP nick-end labeling) staining after 24 h of photothermal treatment (Fig. 5c). In the **BDP2-NPs** + laser group (**BDP2-NPs** + L), massive destruction and apoptosis of tumor tissues were observed compared to the other groups. After laser irradiation, the tumor volume (Fig. 5b and S11†) and body weight (Fig. S12†) of the mice were recorded for 15 consecutive days, and the tumor volume of the **BDP2-NPs** + L group was significantly reduced, which has statistical significance compared with the other groups. However, there was no significant change in body weight, indicating that the photothermal effect of the **BDP2-NPs** could effectively inhibit the growth of tumors in mice without toxicity (Fig. S12†). To further verify the biocompatibility of **BDP2**, different groups were injected with 100 μL of **BDP2-NPs**/PBS through the tail vein. After 36 h, the laser group adopted same irradiation conditions as before. Then, 48 h after the end of the laser irradiation, the mice were sacrificed, serum was taken to detect ALT, AST, BUN, and CREA, and organs were harvested for H&E staining analysis (Fig. S13†). The results show that **BDP2-NPs** itself has no obvious toxicity toward mice, and the photothermal effect of the **BDP2-NPs** will not have adverse effects on mice. All these results indicate that the **BDP2-NPs** successfully inhibit tumor proliferation, show excellent PTT effect, and possess significant advantages in tumor localization and treatment at the *in vivo* level.

Conclusions

We have rationally designed a molecular platform based on 3,5-dithienyl-Aza-BODIPY and investigated strategies for accurately constructing aggregates using substituents with different electronic effects. Photophysical property investigations and single-crystal structure analysis have demonstrated that interactions within and between D–A–D structures significantly contribute to the formation of J aggregates. Additionally, the 3,5-position thiophene unit plays a crucial role in this aggregation process. By employing a D–A–D architecture, we have achieved CT-coupled J-aggregation based on a BODIPY chromophore for the first time. The CT-coupled J-aggregates showed excellent biocompatibility, NIR PA imaging capability for tumor diagnosis, and high PTT performance in *in vitro* and *in vivo* studies. Our research provides valuable insights into the rational design of a CT-coupled J-aggregation platform, paving the way for exploring organic NIR photothermal agents for biophotonics applications.

Ethical statement

All animal experiments were conducted in accordance with the approved agreement of the Institutional Animal Ethics Committee of China Pharmaceutical University (approval code: 2022-12-021). Furthermore, all laboratory animal procedures strictly adhered to the guidelines outlined in the National Institutes of Health Guide for the Care and Use of Laboratory Animals.

Data availability

The ESI† includes all experimental details, including TD-DFT calculations, spectroscopic measurements, synthesis and characterization of all products reported in this study. NMR spectra of all products are included as well.

Author contributions

Conceptualization: S. W., L. G. and H. L; methodology: S. W. and W. Z.; investigation: C. L. and W. C.; visualization: Z. N. and H. L.; supervision: L. G., J. T. and H. L.; writing—original draft: H. L., J. T. and L. G.; writing—review & editing: H. L., J. T. and Z. G. All authors have been involved in checking the data, and have approval the final version of the manuscript.

Conflicts of interest

There are no conflicts to declare.

Acknowledgements

We thank the National Natural Science Foundation of China (No. 21801057, 21871072, and 21775166) for the financial support. Theoretical calculations were carried out at the Computational Centre for Molecular Design of Organosilicon Compounds, Hangzhou Normal University.

Notes and references

1 (*a*) Z. Zeng, S. S. Liew, X. Wei and K. Pu, *Angew. Chem., Int. Ed.*, 2021, **60**, 26454–26475; (*b*) H. S. Jung, P. Verwilst, A. Sharma, J. Shin, J. L. Sessler and J. S. Kim, *Chem. Soc. Rev.*, 2018, **47**, 2280–2297.

2 (*a*) X. Hu, Z. Chen, H. Ao, Q. Fan, Z. Yang and W. Huang, *Adv. Opt. Mater.*, 2022, **10**, 2201067; (*b*) H. Gao, X. Zhi, F. Wu, Y. Zhao, F. Cai, P. Li and Z. Shen, *Angew. Chem., Int. Ed.*, 2023, **62**, e202309208; (*c*) L. Gai, R. Zhang, X. Shi, Z. Ni, S. Wang, J. L. Zhang, H. Lu and Z. Guo, *Chem. Sci.*, 2023, **14**, 1434.

3 S. Xu, H.-W. Liu, S.-Y. Huan, L. Yuan and X.-B. Zhang, *Mater. Chem. Front.*, 2021, **5**, 1076–1089.

4 (*a*) L. Zhao, X. Ren and X. Yan, *CCS Chem.*, 2021, **3**, 678–693; (*b*) N. J. Hestand and F. C. Spano, *Acc. Chem. Res.*, 2017, **50**, 341–350; (*c*) F. Würthner, T. E. Kaiser and C. R. Saha-Möller, *Angew. Chem., Int. Ed.*, 2011, **50**, 3376–3410; (*d*) J. H. Kim, T. Schembri, D. Bialas, M. Stolte and F. Würthner, *Adv. Mater.*, 2022, **34**, 2104678.

5 (*a*) Y. Tian, D. Yin and L. Yan, *Wiley Interdiscip. Rev.: Nanomed. Nanobiotechnol.*, 2023, **15**, e1831; (*b*) J. Heo, D. P. Murale, H. Y. Yoon, V. Arun, S. Choi, E. Kim, J.-S. Lee and S. Kim, *Aggregate*, 2022, **3**, e159.

6 C. Spitz, J. Knoester, A. Ouart and S. Daehne, *Chem. Phys.*, 2002, **275**, 271–284.
7 C. A. Steinbeck, M. Ernst, B. H. Meier and B. F. Chmelka, *J. Phys. Chem. C*, 2008, **112**, 2565–2573.
8 N. J. Hestand, C. Zheng, A. R. Penmetcha, B. Cona, J. A. Cody, F. C. Spano and C. J. Collison, *J. Phys. Chem. C*, 2015, **119**, 18964–18974.
9 (*a*) N. J. Hestand and F. C. Spano, *Chem. Rev.*, 2018, **118**, 7069–7163; (*b*) N. J. Hestand and F. C. Spano, *Chem. Phys.*, 2016, **481**, 262–271.
10 (*a*) C.-A. Shen, D. Bialas, M. Hecht, V. Stepanenko, K. Sugiyasu and F. Würthner, *Angew. Chem., Int. Ed.*, 2021, **60**, 11949–11958; (*b*) A. Kaczmarek-Kedziera and D. Kędziera, *Theor. Chem. Acc.*, 2016, **135**, 214; (*c*) K. Ilina, W. M. MacCuaig, M. Laramie, J. N. Jeouty, L. R. McNally and M. Henary, *Bioconjugate Chem.*, 2020, **31**, 194–213.
11 (*a*) H. Lu, J. Mack, Y. Yang and Z. Shen, *Chem. Soc. Rev.*, 2014, **43**, 4778–4823; (*b*) N. Boens, B. Verbelen, M. J. Ortiz, L. Jiao and W. Dehaen, *Coord. Chem. Rev.*, 2019, **399**, 213024; (*c*) W. Sheng, F. Lv, B. Tang, E. Hao and L. Jiao, *Chin. Chem. Lett.*, 2019, **30**, 1825–1833; (*d*) Z. Shi, X. Han, W. Hu, H. Bai, B. Peng, L. Ji, Q. Fan, L. Li and W. Huang, *Chem. Soc. Rev.*, 2020, **49**, 7533–7567.
12 Z. Chen and Z. Chen, *Org. Chem. Front.*, 2023, **10**, 2581–2602.
13 L. Jing, Y. Zhang, X. Ren and Z. Chen, *Angew. Chem., Int. Ed. Engl.*, 2021, **38**, 10–19.
14 (*a*) M. H. Y. Cheng, K. M. Harmatys, D. M. Charron, J. Chen and G. Zheng, *Angew. Chem., Int. Ed.*, 2019, **58**, 13394–13399; (*b*) B. Lei, H. Pan, Y. Zhang, X.-K. Ren and Z. Chen, *Org. Biomol. Chem.*, 2021, **19**, 6108–6114; (*c*) D. Tian, H. Pan, Y. Zhang, X.-K. Ren and Z. Chen, *Tetrahedron Lett.*, 2021, **76**, 153216.
15 (*a*) Y. Tian, D. Yin, Q. Cheng, H. Dang, C. Teng and L. Yan, *J. Mater. Chem. B*, 2022, **10**, 1650–1662; (*b*) X. Guo, J. Yang, M. Li, F. Zhang, W. Bu, H. Li, Q. Wu, D. Yin, L. Jiao and E. Hao, *Angew. Chem., Int. Ed.*, 2022, **61**, e202211081; (*c*) W. Sheng, Z. Wang, E. Hao and L. Jiao, *Chin. Chem. Lett.*, 2021, **32**, 1249–1252.
16 C. Gustafsson, H. Shirani, P. Leira, D. R. Rehn, M. Linares, K. P. R. Nilsson, P. Norman and M. Lindgren, *ChemPhysChem*, 2021, **22**, 323–335.
17 M. J. Frisch, G. W. Trucks, H. B. Schlegel, G. E. Scuseria, M. A. Robb, J. R. Cheeseman, G. Scalmani, V. Barone, G. A. Petersson, H. Nakatsuji, X. Li, M. Caricato, A. V. Marenich, J. Bloino, B. G. Janesko, R. Gomperts, B. Mennucci, H. P. Hratchian, J. V. Ortiz, A. F. Izmaylov, J. L. Sonnenberg, D. Williams-Young, F. Ding, F. Lipparini, F. Egidi, J. Goings, B. Peng, A. Petrone, T. Henderson, D. Ranasinghe, V. G. Zakrzewski, J. Gao, N. Rega, G. Zheng, W. Liang, M. Hada, M. Ehara, K. Toyota, R. Fukuda, J. Hasegawa, M. Ishida, T. Nakajima, Y. Honda, O. Kitao, H. Nakai, T. Vreven, K. Throssell, J. A. Montgomery Jr, J. E. Peralta, F. Ogliaro, M. J. Bearpark, J. J. Heyd, E. N. Brothers, K. N. Kudin, V. N. Staroverov, T. A. Keith, R. Kobayashi, J. Normand, K. Raghavachari, A. P. Rendell, J. C. Burant, S. S. Iyengar, J. Tomasi, M. Cossi, J. M. Millam, M. Klene, C. Adamo, R. Cammi, J. W. Ochterski, R. L. Martin, K. Morokuma, O. Farkas, J. B. Foresman and D. J. Fox, *Gaussian 16 (Revision A.03)*, Gaussian Inc., Wallingford, CT, 2016.
18 (*a*) X. Zhang, H. Yu and Y. Xiao, *J. Org. Chem.*, 2012, **77**, 669–673; CCDC no. 877767–877768. Reproduced with permission.; (*b*) R. Gresser, H. Hartmann, M. Wrackmeyer, K. Leo and M. Riede, *Tetrahedron*, 2011, **67**, 7148–7155; (*c*) A. E. Pogonin, A. Y. Shagurin, M. A. Savenkova, F. Y. Telegin, Y. S. Marfin and A. S. Vashurin, *Molecules*, 2020, **25**, 5361.
19 (*a*) Y. Ge and D. F. O'Shea, *Chem. Soc. Rev.*, 2016, **45**, 3846–3864; (*b*) G. Kubheka, J. Mack, T. Nyokong and Z. Shen, *Molecules*, 2020, **25**, 3689; (*c*) Y. Wang, D. Zhang, K. Xiong, R. Shang and X.-D. Jiang, *Chin. Chem. Lett.*, 2022, **33**, 115–122.
20 (*a*) P. Jonkheijm, P. van der Schoot, A. P. H. J. Schenning and E. W. Meijer, *Science*, 2006, **313**, 80–83; (*b*) Z. Chen, Y. Liu, W. Wagner, V. Stepanenko, X. Ren, S. Ogi and F. Würthner, *Angew. Chem., Int. Ed.*, 2017, **56**, 5729–5733; (*c*) X. Wang, Z. Jiang, Z. Liang, T. Wang, Y. Chen and Z. Liu, *Sci. Adv.*, 2022, **8**, eadd5660.
21 (*a*) E.-K. Lim, T. Kim, S. Paik, S. Haam, Y.-M. Huh and K. Lee, *Chem. Rev.*, 2015, **115**, 327–394; (*b*) J. Shi, P. W. Kantoff, R. Wooster and O. C. Farokhzad, *Nat. Rev. Cancer*, 2017, **17**, 20–37.
22 D. K. Roper, W. Ahn and M. Hoepfner, *J. Phys. Chem. C*, 2007, **111**, 3636–3641.
23 (*a*) X. Song, L. Feng, C. Liang, K. Yang and Z. Liu, *Nano Lett.*, 2016, **16**, 6145–6153; (*b*) J. Jo, C. H. Lee, R. Kopelman and X. Wang, *Nat. Commun.*, 2017, **8**, 471.